biosensors

MDPI

Article

COMSOL-Based Impedance and Sensitivity Analysis of an Interdigitated Electrode Biosensor for Dengue NS1 Detection

Saleh I. Alzahrani

Biomedical Engineering Department, College of Engineering, Imam Abdulrahman Bin Faisal University, P.O. Box 1982, Dammam 31451, Saudi Arabia; sialzahrani@iau.edu.sa

Abstract

Dengue remains a major global public health concern, highlighting the need for rapid and sensitive methods for the early detection of dengue virus biomarkers. In the present study, a finite element model for the detection of dengue nonstructural protein 1 (NS1) using an interdigitated electrode (IDE)-based impedimetric biosensor was developed in COMSOL Multiphysics. The proposed sensor consists of gold IDEs coated with an antibody-based biorecognition layer and immersed in a conductive aqueous sample medium. Antibody–NS1 binding was modeled using the Langmuir adsorption isotherm. Frequency-domain simulations were used to examine the impedance response over a range of NS1 concentrations from 0 to 1000 ng/cm^3. The results showed that the simulated impedance magnitude decreased with increasing NS1 concentration and excitation frequency. At 10 MHz, the normalized impedance response increased rapidly at low NS1 concentrations and gradually approached saturation at higher concentrations. A linear fit to three simulated concentration points (1–3 ng/cm^3) yielded a normalized response slope of 0.9223%/(ng/cm^3) ($R^2 = 0.9963$), providing a preliminary characterization of the model-predicted low-concentration response. These findings demonstrate the potential of computational modeling for characterizing the predicted electrical response of an IDE-based impedimetric NS1 biosensor, providing a basis for sensor optimization and future experimental validation. The reported sensitivity and concentration-dependent responses are simulation-based predictions and have not been experimentally validated.

Keywords: dengue NS1; impedimetric biosensor; interdigitated electrodes; electrochemical impedance spectroscopy; Langmuir adsorption model; COMSOL Multiphysics

1. Introduction

Dengue is a mosquito-borne viral infection caused by the dengue virus (DENV), a single-stranded RNA (ssRNA) virus belonging to the genus *Orthoflavivirus* within the *Flaviviridae* family [1,2]. Dengue poses a major global health concern, particularly in tropical and subtropical regions worldwide. The World Health Organization (WHO) estimates that around 100–400 million infections occur annually, of which approximately 70% are asymptomatic [3,4]. This highlights the importance of timely and accurate diagnosis of dengue infection to support appropriate clinical management and reduce the morbidity and mortality associated with dengue hemorrhagic fever (DHF) and dengue shock syndrome (DSS).

Several traditional laboratory-based diagnostic approaches are currently available for detecting dengue infection. These include serological methods such as IgM/IgG antibody testing, nucleic acid-based methods such as polymerase chain reaction (PCR), and antigen

Check for updates

Received: 30 September 2026
Revised: 26 October 2026
Accepted: 30 October 2026
Published: 1 November 2026

Copyright: © 2026 by the author. Licensee MDPI, Basel, Switzerland. This article is an open access article distributed under the terms and conditions of the Creative Commons Attribution (CC BY) license.

detection methods [5–7]. Nonstructural protein 1 (NS1) antigen detection has emerged as a promising approach because it allows for rapid and relatively inexpensive detection during the early phase of infection. In addition, NS1 antigen detection has a reported sensitivity ranging from 63% to 94%, making it particularly suitable for resource-limited healthcare facilities [8].

Recently, biosensing approaches have gained increasing attention in dengue diagnostics by enabling rapid, accurate, and cost-effective detection of the NS1 antigen, an early biomarker of dengue infection. Previous studies have investigated various biosensing platforms for NS1 detection, including electrochemical, optical, microfluidic, and smartphone-based biosensors [9–12]. Due to their high sensitivity, potential for miniaturization, low cost, and versatility, electrochemical biosensors are widely used for detecting low levels of biomarkers [13–15]. Furthermore, electrochemical biosensors can enable label-free detection, reducing reagent consumption and simplifying the detection process [16].

Among the available electrochemical detection methods, electrochemical impedance spectroscopy (EIS) is widely used for label-free biomolecular detection. EIS is a non-destructive analytical technique that measures impedance by applying a small-amplitude AC voltage to an electrochemical system and measuring the resulting current response [17]. For EIS-based impedimetric sensors, interdigitated electrodes (IDEs) are commonly used due to their high sensitivity and ease of miniaturization. The combination of EIS with IDEs has been widely investigated in various biomedical sensing applications, including immunological biomarker detection, cancer diagnostics, bio-affinity sensing, and infectious disease detection [18–21].

In recent years, several studies have investigated the use of impedimetric biosensors for dengue diagnosis through the detection of the NS1 antigen using anti-NS1 antibodies. For example, Cecchetto et al. developed a label-free impedimetric biosensor using anti-NS1 antibodies immobilized on a gold electrode, achieving detection limits of 3 ng/mL in PBS and 30 ng/mL in serum [9]. Similarly, Nawaz et al. developed a portable impedimetric immunosensor based on anti-NS1-modified screen-printed carbon electrodes, with a detection limit of 0.3 ng/mL and a linear range of 1–200 ng/mL for NS1 detection [22]. More recently, Ojha et al. developed a label-free impedimetric immunosensor based on an anti-NS1-functionalized gold nanorod–graphitic carbon nitride-modified electrode, achieving a linear detection range of 0.6–216 ng/mL and a limit of detection (LOD) of 0.09 ng/mL in PBS [23]. Table 1 compares previously reported dengue NS1 biosensors with the present computational study.

Despite these advances, most reported studies have focused on the experimental development and performance evaluation of impedimetric biosensors, while detailed computational investigations of how NS1 concentration alters the interfacial electrical properties of IDE-based sensors remain limited. This highlights the importance of physics-based modeling for understanding how the interfacial impedance response is influenced by NS1 concentration. To address this gap, the present study investigated the impedance response and model-predicted sensitivity of an IDE biosensor for dengue NS1 detection using COMSOL Multiphysics. In addition, this study examined key sensor response characteristics, including linearity, sensitivity, frequency-dependent impedance response, and electric field distribution.

Table 1. Comparison of the present computational study with previously published electrochemical biosensors for dengue NS1 detection.

Study	Electrode Configuration	Sensing Method	NS1 Concentration Range (ng/mL)	Reported Sensitivity	Study Type
Cecchetto et al. (2015) [9]	Anti-NS1-functionalized gold electrode	EIS	10–2000 (PBS); 10–1000 (serum)	14.1%/decade (PBS); 10.4%/decade (serum)	Experimental
Nawaz et al. (2018) [22]	Anti-NS1/BSA-modified screen-printed carbon electrode	EIS	1–200	NR	Experimental
Wasik et al. (2018) [24]	Antibody-functionalized SWNT network on gold IDEs	Chemiresistive	Approximately 1–1000 (artificial saliva)	−4.52 ± 0.13% per log	Experimental
Bachour Junior et al. (2021) [25]	DNA aptamer-functionalized gold electrode	EIS	0.01–1000	2.9, 2.7 and 1.7%/decade, depending on NS1 serotype and sample matrix	Experimental
Ojha et al. (2022) [23]	Anti-NS1-functionalized AuNRs–g-C_3N_4-modified glassy carbon electrode	EIS	0.6–216 (PBS); 3–177 (serum)	NR	Experimental
Sirivibulkovit et al. (2025) [26]	Screen-printed gold electrode (AuSPE) with epitope-imprinted MIP nanoparticles	Differential pulse voltammetry (DPV); competitive and direct assays	5–300 (competitive); 10–100 (direct)	0.053 µA·mL/ng (competitive); 0.044 µA·mL/ng (direct)	Experimental
Present study (2026)	Gold IDE with modeled antibody-functionalized layer	COMSOL frequency-domain impedance simulation	0–1000 simulated; 1–3 fitted	0.9223%/(ng/mL), simulated	Computational

NR = not reported; EIS = electrochemical impedance spectroscopy; IDE = interdigitated electrode; PBS = phosphate-buffered saline.

2. Materials and Methods

2.1. Biosensor Design and Geometry

In this study, finite element analysis (FEA) was performed using COMSOL Multiphysics® (Version 6.3, COMSOL AB, Stockholm, Sweden) to develop and simulate a three-dimensional (3D) model of the proposed IDE-based biosensor for dengue NS1 detection. The model was used to simulate the electrical response of the biosensor in a conductive aqueous sample medium. Figure 1 depicts the main components and geometry of the proposed IDE-based biosensor. The geometrical parameters used in the COMSOL model are summarized in Table 2.

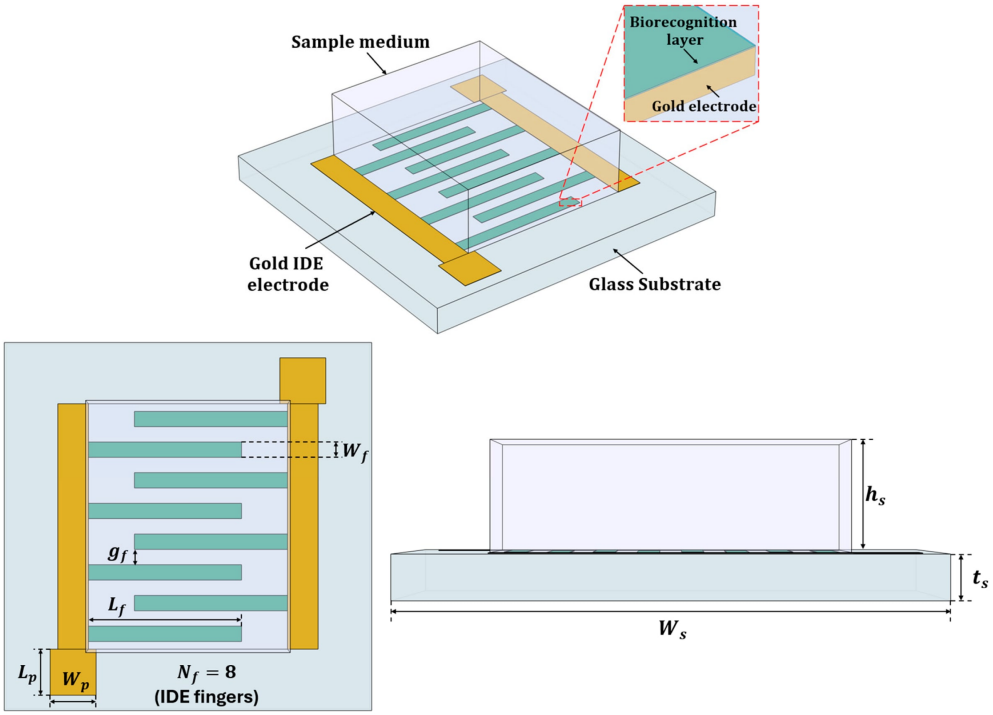


Figure 1. Geometry of the proposed IDE-based biosensor: (**top**) three-dimensional configuration, (**bottom left**) top view showing the IDE geometrical parameters, and (**bottom right**) side view showing the vertical dimensions of the sensor structure.

Table 2. Geometrical parameters of the proposed IDE-based biosensor.

Parameter	Symbol	Value
Substrate width	w_s	200 µm
Substrate thickness	t_s	20 µm
IDE finger width	w_f	10 µm
IDE finger length	L_f	100 µm
Inter-finger gap	g_f	10 µm
Gold electrode thickness	t_e	0.2 µm
Biorecognition layer thickness	t_b	0.01 µm
Sample medium height	h_s	50 µm
Number of IDE fingers	N_f	8
Contact pad width	w_p	30 µm
Contact pad length	L_p	30 µm
Contact pad thickness	t_p	0.2 µm

A gold IDE was modeled on a glass substrate with a width of 200 µm and a thickness of 20 µm and covered by a biorecognition layer, as illustrated in Figure 1. The gold IDEs were patterned on the substrate, with each electrode finger having a width, length, and thickness of 10 µm, 100 µm, and 0.2 µm, respectively. The gap between adjacent fingers was set at a constant distance of 10 µm, and a total of eight interdigitated fingers were used in the sensor geometry. A thin biorecognition layer with a thickness of 0.01 µm was positioned directly above the gold electrode surfaces to represent the antibody-functionalized sensing interface. The IDE structure and biorecognition layer were covered by a sample medium with a height of 50 µm. Each contact pad had dimensions of 30 µm × 30 µm, with a thickness of 0.2 µm.

2.2. COMSOL Multiphysics Electrical Model

The Electric Currents (EC) physics interface in COMSOL Multiphysics was used to model the electric field and electric potential distributions within the IDE-based biosensor in the frequency domain. The governing equations used for the electric field and electric potential are expressed as follows:

$$E = -\nabla V \tag{1}$$

where E is the electric field and V is the electric potential.

$$J = (\sigma + j\omega\varepsilon)E \tag{2}$$

where J is the current density, σ is the electrical conductivity, ε is the permittivity, $j = \sqrt{-1}$ is the imaginary unit, and $\omega = 2\pi f$ is the angular frequency.

The conservation of electric current is expressed as

$$\nabla \cdot J = 0 \tag{3}$$

Accordingly, the electric potential distribution was obtained by solving the time-harmonic current continuity equation [27]:

$$\nabla \cdot [-(\sigma + j\omega\varepsilon)\nabla V] = 0 \tag{4}$$

2.3. Antibody–NS1 Langmuir Binding Model

The Langmuir binding model was used to describe the specific binding of dengue NS1 antigen to the immobilized anti-NS1 antibodies in the biorecognition layer. The model is based on the assumption of 1:1 binding between the target antigen and homogeneous, independent binding sites on the antibody-functionalized surface. This approach has been applied to the characterization of anti-dengue NS1 antibody binding using surface plasmon resonance and other label-free biosensing techniques and has also been used to describe protein–antibody interactions in biosensing systems [28–30].

The Langmuir isotherm was used to calculate the fractional occupancy of the available antibody binding sites [31]:

$$\theta_{NS1} = \frac{C_{NS1}}{K_{D,NS1} + C_{NS1}} \tag{5}$$

where θ_{NS1} is the fractional occupancy of antibody binding sites, C_{NS1} is the NS1 concentration, and $K_{D,NS1}$ is the equilibrium dissociation constant. The Langmuir relationship predicts that as antigen concentration increases, surface occupancy increases and approaches saturation at high antigen concentrations. When $C_{NS1} = K_{D,NS1}$, half of the available binding sites are occupied ($\theta_{NS1} = 0.5$).

In the present model, the equilibrium dissociation constant (K_D) was assumed to be 10 ng/cm^3 as a representative modeling parameter rather than an experimentally determined binding affinity. The Langmuir model assumes equilibrium binding and uniform surface coverage. Time-dependent binding kinetics and mass-transfer limitations were not explicitly considered; therefore, the model does not predict the time required to reach equilibrium.

To account for the effect of NS1 binding on the electrical response, the effective conductivity and relative permittivity of the biorecognition layer were assumed to vary linearly with the fractional occupancy calculated using the Langmuir model. These properties were interpolated between the defined unbound and fully bound states as follows:

$$\sigma_{\text{bio}} = (1 - \theta_{\text{NS1}})\sigma_{\text{bio,free}} + \theta_{\text{NS1}}\sigma_{\text{bio,bound}} \tag{6}$$

$$\varepsilon_r = (1 - \theta_{\text{NS1}})\varepsilon_{r,\text{bio,free}} + \theta_{\text{NS1}}\varepsilon_{r,\text{bio,bound}} \tag{7}$$

where $\sigma_{bio,free}$ and $\sigma_{bio,bound}$ denote the electrical conductivities of the unbound and NS1-bound biorecognition layers, respectively. Similarly, $\varepsilon_{r,bio,free}$ and $\varepsilon_{r,bio,bound}$ represent their corresponding relative permittivities. In the present model, $\sigma_{bio,free}$ and $\sigma_{bio,bound}$ were set to 1×10^{-4} and 2×10^{-4} S/m, respectively, whereas $\varepsilon_{r,bio,free}$ and $\varepsilon_{r,bio,bound}$ were set to 4 and 6, respectively. As described by the Langmuir relationship, the simulated fractional occupancy increased with increasing NS1 concentration, gradually changing the effective electrical properties of the biorecognition layer, which were subsequently incorporated into the frequency-domain impedance simulations. Physically, NS1 binding may alter the effective electrical properties of the biorecognition layer through changes in interfacial charge distribution, local hydration, and dielectric polarization. In the present model, these effects are represented collectively through the assumed occupancy-dependent conductivity and permittivity, without explicitly modeling individual molecular mechanisms or changes in layer thickness. The linear interpolation was adopted as a first-order phenomenological approximation between the unbound and fully bound states, assuming that the effective changes in conductivity and permittivity are proportional to antibody binding-site occupancy. This approach provides a consistent coupling between the Langmuir binding model and the frequency-domain electrical simulations while maintaining a fixed biorecognition-layer thickness.

Antibody–NS1 binding was represented through concentration-dependent electrical properties of the biorecognition layer rather than an explicit surface reaction. For each NS1 concentration, the equilibrium fractional occupancy was used to update the conductivity and relative permittivity of the biorecognition layer before performing the frequency-domain simulation. No additional binding-reaction or mass-transport boundary conditions were imposed.

The coupling between NS1 binding and the electrical response was implemented through changes in the effective conductivity and relative permittivity of the biorecognition layer. As NS1 concentration increases, the Langmuir model predicts greater antibody binding-site occupancy, which modifies these electrical properties according to Equations (6) and (7). The resulting changes affect the conductive and capacitive current distributions near the IDE surfaces, particularly within the high-electric-field regions between adjacent electrode fingers, thereby altering the total terminal current and the calculated impedance. This mechanism represents an assumed phenomenological relationship between biomolecular binding and electrical properties rather than an experimentally established interaction.

2.4. Electrical Properties and Boundary Conditions

The electrical properties of the computational domains were defined in terms of electrical conductivity, σ, and relative permittivity, ε_r. The glass substrate was treated as an insulating (dielectric) material, while the IDEs were assigned the electrical properties of gold. The sample medium was modeled as a conductive aqueous medium, with an assumed relative permittivity of 78 and an electrical conductivity of 1.5 S/m, consistent with values reported in previous computational studies [32,33]. The fractional antibody–NS1 binding occupancy presented in the previous section was used to determine the concentration-dependent electrical properties of the biorecognition layer using assumed unbound and fully bound material properties. The electrical properties of the different computational domains are summarized in Table 3.

Table 3. Electrical Properties of the Materials Used in the COMSOL Model.

Computational Domain	Electrical Conductivity, σ (S/m)	Relative Permittivity, ε_r
Glass substrate	1×10^{-12}	4.7
Gold IDEs	4.1×10^{7}	1
Dengue sample medium	1.5	78
Biorecognition layer (unbound)	1×10^{-4}	4
Biorecognition layer (fully bound)	2×10^{-4}	6

For electrical excitation, one IDE was connected to a sinusoidal voltage with an amplitude of 10 mV using the Terminal boundary condition, while the other electrode was set to ground using the Ground boundary condition. The applied voltage was defined as:

$$V_{\text{terminal}} = V_{\text{exc}} = 10\ \text{mV}, V_{\text{ground}} = 0\ \text{V} \tag{8}$$

The remaining external boundaries were treated as electrically insulating, such that no normal current flowed across these boundaries, as expressed by:

$$n \cdot J = 0 \tag{9}$$

where n is the outward unit normal vector and J is the current density. These boundary conditions were applied to the modeled sensor and sample domain to confine the electrical response to the computational domain and allow the calculation of the frequency-dependent potential and current distributions.

The complex impedance of the biosensor was determined from the applied terminal voltage and the resulting total current as follows:

$$Z(f) = \frac{V_{\text{exc}}(f)}{I_{\text{terminal}}(f)} \tag{10}$$

where $Z(f)$ is the complex impedance, $V_{\text{exc}}(f)$ is the applied voltage, and $I_{\text{terminal}}(f)$ is the resulting terminal current at frequency f. The impedance magnitude was subsequently calculated as follows:

$$|\, Z(f) \,| = \sqrt{[\text{Re}(Z(f))]^2 + [\text{Im}(Z(f))]^2} \tag{11}$$

The frequency-dependent electrical response of the IDE biosensor was obtained at different NS1 concentrations and characterized using the calculated impedance.

2.5. Frequency-Domain Simulation and Sensitivity Analysis

A frequency-domain parametric study was carried out to investigate the effect of NS1 concentration on the electrical response of the proposed IDE-based biosensor. The NS1 concentration, C_{NS1}, was varied over a wide concentration range from 0 to 1000 ng/cm^3, using the following values: 0, 1, 2, 3, 4, 5, 6, 7, 8, 9, 10, 25, 50, 100, 250, 500, and 1000 ng/cm^3. The fractional antibody–NS1 binding occupancy, θ_{NS1}, was calculated for each concentration based on the Langmuir binding model. The electrical properties of the biorecognition layer were then updated accordingly.

To characterize the frequency-dependent impedance response of the biosensor, a frequency-domain simulation was performed for each NS1 concentration over the specified frequency range. The complex impedance and impedance magnitude were computed from the applied terminal voltage and resulting terminal current. The obtained impedance spectra were used to study the effects of both excitation frequency and NS1 concentration on the sensor response. The electric potential and electric field distributions were also analyzed to investigate the electrical behavior in the sensing region.

The biosensor response was studied as a function of NS1 concentration using the impedance magnitude at 10 MHz. The impedance response was normalized to the baseline condition ($C_{NS1} = 0$), and the relationship between NS1 concentration and the simulated normalized impedance response was examined. The normalized impedance response was calculated as follows:

$$R_Z(C_{\mathrm{NS1}}) = \frac{|Z_0| - |Z(C_{\mathrm{NS1}})|}{|Z_0|} \times 100\% \quad (12)$$

where $|Z_0|$ is the impedance magnitude at zero NS1 concentration, and $|Z(C_{\mathrm{NS1}})|$ is the impedance magnitude at the specified NS1 concentration.

3. Results

3.1. Electric Potential and Electric Field Distribution

Figure 2 shows the electric potential and electric field distributions of the IDE-based biosensor at an NS1 concentration of 10 ng/cm^3 and an excitation frequency of 10 MHz. The electric potential varied between the excited and grounded electrodes, creating alternating regions of high and low electric potential around the interdigitated fingers (see Figure 2a). The potential gradient was pronounced in the gaps between adjacent electrode fingers, suggesting that these areas play a significant role in the electrical interaction with the biorecognition layer and the surrounding sample medium.

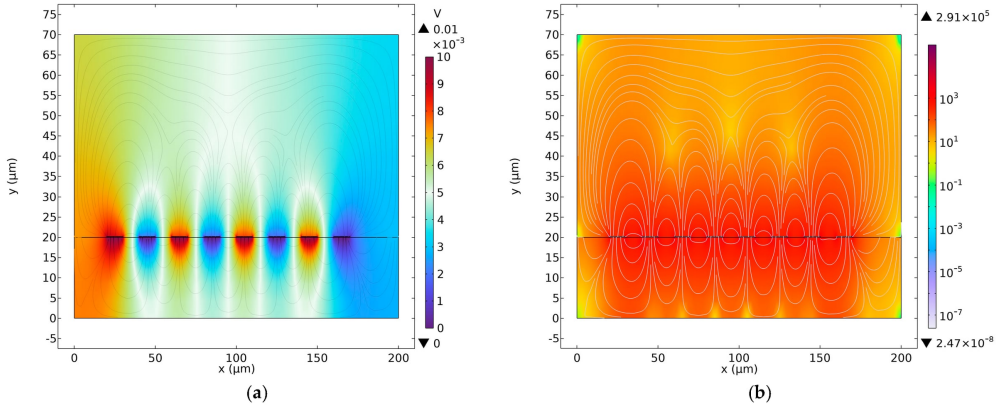


Figure 2. Simulated distributions of (**a**) electric potential and (**b**) electric field magnitude with overlaid field lines in the IDE-based biosensor at an NS1 concentration of 10 ng/cm^3 and an excitation frequency of 10 MHz.

Figure 2b shows the electric field magnitude and field lines. The maximum simulated electric field magnitude was approximately 2.91 × 10^5 V/m and occurred near the IDE fingers, particularly at the electrode edges and in the gaps between them. The field lines extended from the electrode region into the sample medium, indicating electric field fringing in the sensing region. The proposed sensing mechanism relies on changes in the electrical properties of the antibody–NS1 biorecognition layer, and these changes can influence the impedance response in the high-field regions near the electrode surfaces. The electric field magnitude in Figure 2b is plotted on a logarithmic scale to illustrate the field distribution over its wide dynamic range.

To evaluate the electric field penetration depth, the electric field magnitude was extracted along a vertical line extending from the sensing surface into the sample medium at the center of an inter-electrode gap (Figure 3a). At 10 MHz and 0 ng/cm^3 NS1 concentration, the electric field decreased from approximately 484.61 V/m at the sensing surface to 36.8% (1/e) of its initial value at a distance of approximately 8.82 µm, corresponding to the characteristic penetration depth along the selected vertical line. This characteristic penetration depth is substantially greater than the biorecognition layer thickness of 0.01

μm, indicating that the electric field extends beyond the sensing layer into the surrounding sample medium.

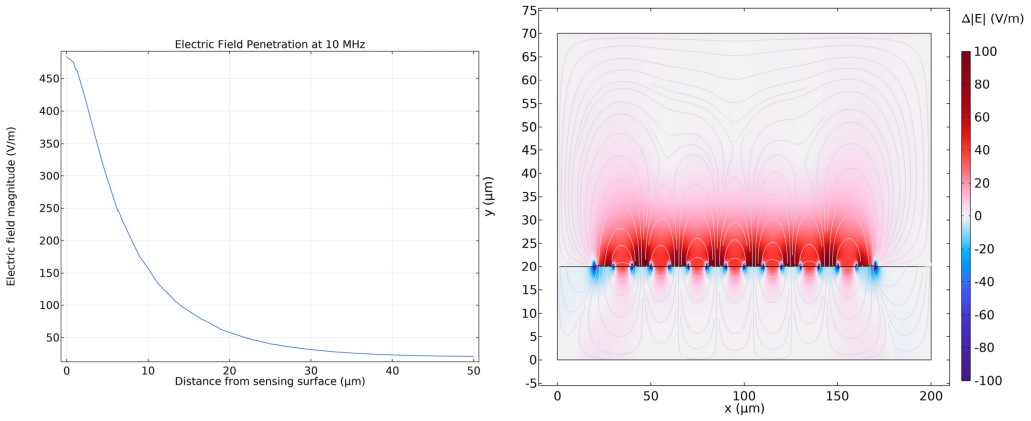


Figure 3. Electric field analysis at 10 MHz: (**a**) electric field magnitude as a function of vertical distance from the sensing surface at 0 ng/cm^3 NS1 concentration, showing a characteristic penetration depth of approximately 8.82 μm; (**b**) spatial distribution of the electric field magnitude difference between 1000 and 0 ng/cm^3 NS1 concentrations.

To investigate the influence of NS1 concentration on the electric field distribution, the difference in electric field magnitude between 1000 and 0 ng/cm^3 was evaluated at 10 MHz, as shown in Figure 3b. The results reveal spatially nonuniform changes, with localized increases and decreases in electric field magnitude primarily near the electrode edges and inter-electrode gaps. At a representative location near the electrode surface (x = 25 μm, y = 20.22 μm), the electric field magnitude increased from 309.80 to 374.56 V/m, corresponding to a 20.9% increase.

3.2. Frequency-Dependent Impedance Response

Figure 4 shows the simulated impedance magnitude as a function of frequency for representative NS1 concentrations ranging from 0 to 1000 ng/cm^3. The impedance magnitude at low and intermediate frequencies was relatively constant. Moreover, the results showed distinct impedance values at different NS1 concentrations. The impedance magnitude decreased with increasing NS1 concentration, and this trend was observed across the investigated frequency range. This behavior resulted in changes in the electrical properties of the biorecognition layer introduced by the antibody–NS1 binding model.

The impedance magnitude decreased significantly at higher frequencies, with a more pronounced decrease in the MHz range. This frequency-dependent behavior is consistent with the increasing contribution of capacitive current as the excitation frequency increases. The separation between the curves was maintained up to 10 MHz despite the overall decrease in impedance. The highest impedance was obtained for the baseline condition ($C_{NS1} = 0$), and the impedance subsequently decreased with increasing NS1 concentration. The decrease became less pronounced at higher NS1 concentrations, consistent with the saturation behavior predicted by the Langmuir binding model. Based on the maintained concentration-dependent response at the upper end of the investigated frequency range, the impedance magnitude at 10 MHz was selected to evaluate the concentration-dependent response and sensitivity of the biosensor. The selection of 10 MHz was based on the maintained separation between the simulated impedance responses at different NS1 concentrations within the investigated frequency range. However, this frequency was selected for evaluating the concentration-dependent response and was not established as the optimal operating frequency. Although larger absolute impedance differences were observed at

lower frequencies, the present study selected 10 MHz as a representative frequency at which concentration-dependent responses remained distinguishable despite the increased capacitive contribution. A systematic comparison of frequency-dependent sensitivity, measurement noise, and signal-to-noise ratio was beyond the scope of the present simulations and is required to determine the optimal operating frequency experimentally.

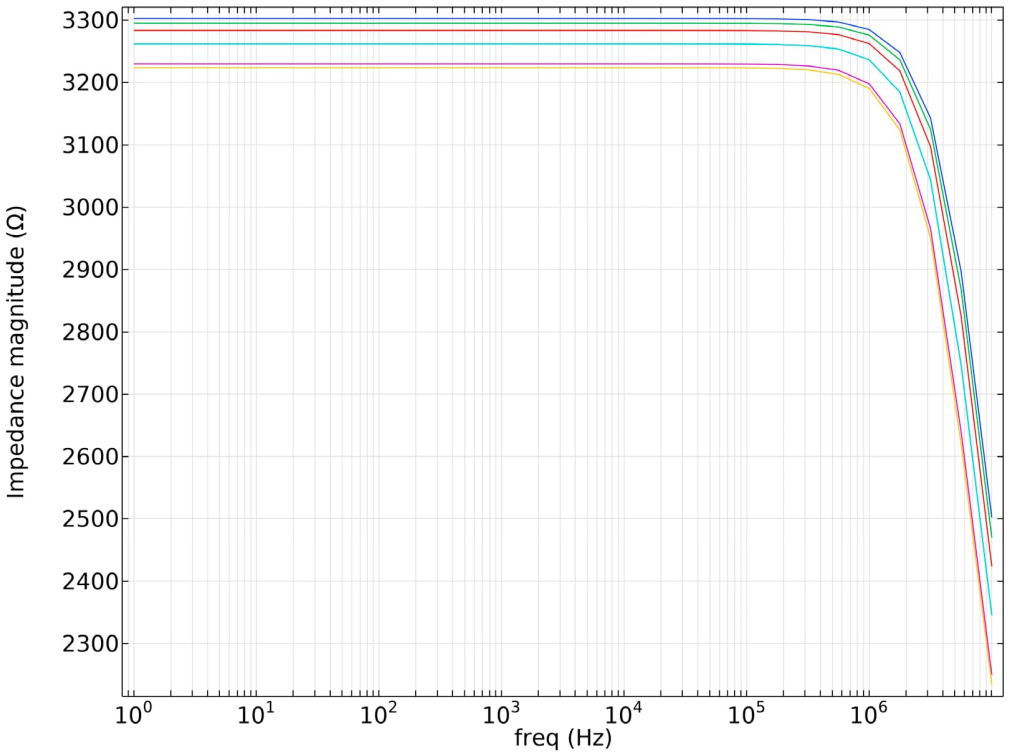


Figure 4. Simulated impedance magnitude as a function of excitation frequency for representative NS1 concentrations of 0, 1, 3, 10, 100, and 1000 ng/cm^3, selected from the 17 simulated concentrations for clarity.

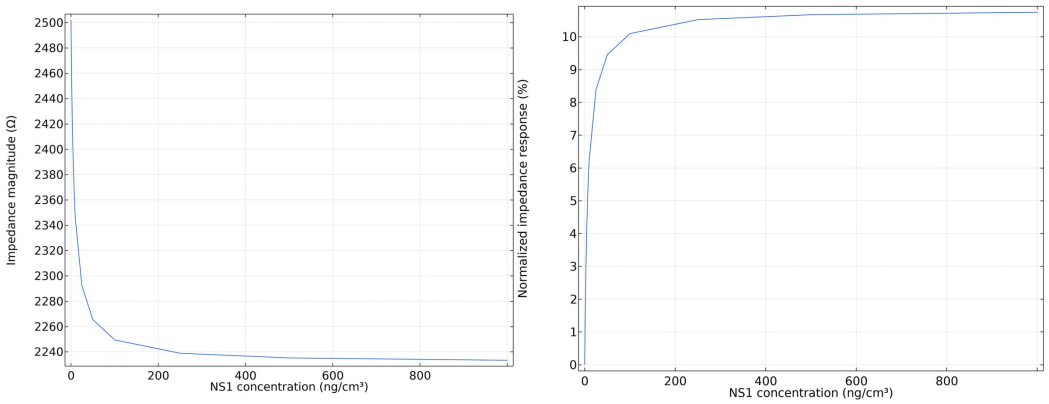
3.3. NS1 Concentration-Dependent Impedance Response

It was observed that the impedance magnitude of the proposed IDE biosensor decreased progressively with increasing NS1 concentration, from approximately 2502 Ω in the absence of NS1 to approximately 2233 Ω at 1000 ng/cm^3, as shown in Figure 5a. The largest changes in impedance were observed at relatively low NS1 concentrations.

The impedance values were normalized to the baseline impedance at C_{NS1} = 0 ng/cm^3 to further characterize the concentration-dependent response. The normalized impedance response increased rapidly at low NS1 concentrations and then gradually leveled off at higher concentrations, reaching approximately 10.7% at 1000 ng/cm^3, as shown in Figure 5b. This nonlinear saturation behavior is consistent with the Langmuir model, which describes antigen concentration-dependent antibody binding.

At low antigen concentrations, the fraction of occupied antibody binding sites increases rapidly, whereas at higher NS1 concentrations, the fractional occupancy approaches unity. For the assumed equilibrium dissociation constant of 10 ng/cm^3, the Langmuir model predicts approximately 50%, 90.9%, and 99.0% binding-site occupancy at NS1 concentrations of 10, 100, and 1000 ng/cm^3, respectively. Consequently, as the available binding sites approach saturation, further increases in NS1 concentration produce progressively smaller changes in the effective electrical properties of the biorecognition layer, resulting in a reduced incremental impedance response and the observed plateau. The corresponding Langmuir binding-site occupancy curve is presented in Figure 6, illustrating the progressive saturation

of available antibody binding sites with increasing NS1 concentration. The pronounced response at low concentrations was further investigated to determine the linear range and sensitivity of the proposed sensor.



(**a**) (**b**)

Figure 5. Simulated NS1 concentration-dependent impedance response of the IDE-based biosensor at 10 MHz: (**a**) impedance magnitude as a function of NS1 concentration and (**b**) normalized impedance response as a function of NS1 concentration, with the baseline condition ($C_{NS1} = 0$ ng/cm^3) corresponding to 0% response.

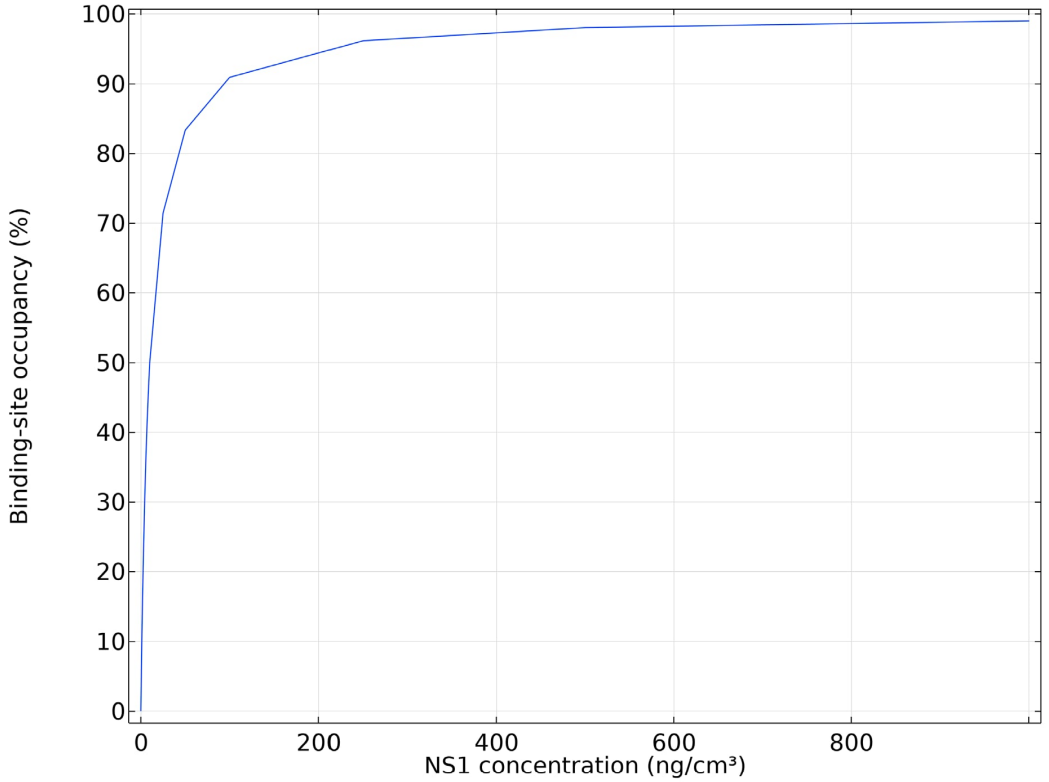


Figure 6. Model-predicted antibody binding-site occupancy as a function of dengue NS1 concentration, calculated using the Langmuir equilibrium binding model with an assumed dissociation constant of 10 ng/cm^3. The fractional occupancy approaches saturation at higher NS1 concentrations.

3.4. Sensitivity and Linear Range

The normalized impedance response at 10 MHz was used to evaluate the sensitivity and linear range of the proposed IDE biosensor. As shown in Figure 7, the simulated responses at

NS1 concentrations of 1, 2, and 3 ng/cm^3 were 1.2879%, 2.3075%, and 3.1324%, respectively. Over this concentration range, the following linear regression equation was obtained:

$$R_Z = 0.9223C_{NS1} + 0.3981 \quad (13)$$

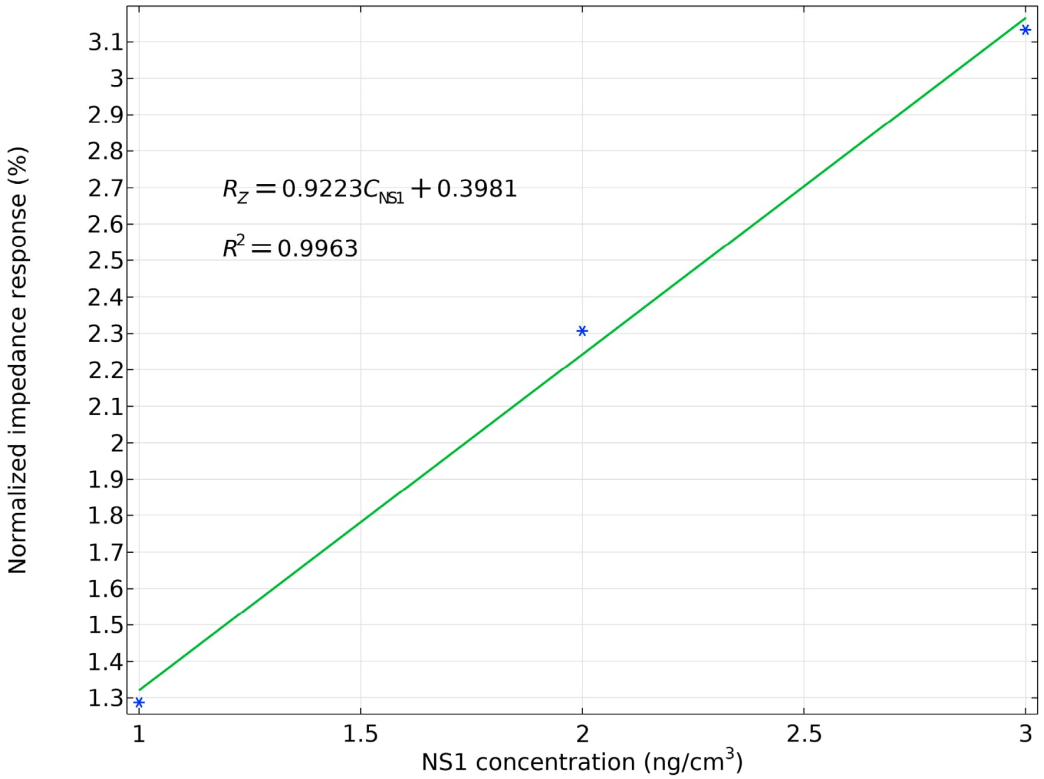


Figure 7. Normalized impedance response as a function of NS1 concentration over the range of 1–3 ng/cm^3 at 10 MHz. The asterisks (*) indicate the COMSOL simulation results, and the solid line represents the linear regression fit.

The coefficient of determination (R^2) was 0.9963. The sensitivity, determined from the slope of the regression line, was 0.9223%/(ng/cm^3). The high R^2 value indicates a strong linear relationship between the normalized impedance response and NS1 concentration over the evaluated range. Outside this low-concentration region, the incremental response decreased as NS1 concentration increased, and the concentration–response curve gradually approached a plateau. Therefore, the 1–3 ng/cm^3 interval was used to characterize the local slope of the simulated low-concentration response rather than to establish a statistically validated linear operating range.

To further evaluate the selection of the linear calibration interval, regression analyses were performed over progressively wider NS1 concentration ranges. Extending the interval from 1–3 to 1–5 ng/cm^3 reduced the coefficient of determination from 0.9963 to 0.9871 and the fitted sensitivity from 0.9223 to 0.7698%/(ng/cm^3). Further extension to 1–10 ng/cm^3 reduced the coefficient of determination to 0.9589, indicating increasing deviation from linear behavior. Accordingly, the 1–3 ng/cm^3 interval was retained as a conservative, model-predicted low-concentration calibration range with high fitted sensitivity. Although the 1–4 ng/cm^3 interval also exhibited strong linearity (R^2 = 0.9918), the narrower interval was selected to prioritize higher fitted sensitivity and lower deviation from linearity, rather than to establish 3 ng/cm^3 as a strict upper limit of linearity. This interval should not be interpreted as the experimentally established analytical working range of a fabricated sensor. The regression results for the different concentration intervals are summarized in Table 4.

Table 4. Comparison of model-predicted linear regression performance over selected NS1 concentration intervals at 10 MHz, showing fitted sensitivity, coefficient of determination (R^2), and maximum normalized deviation from the fitted regression line.

Concentration Interval (ng/cm^3)	Sensitivity (%/(ng/cm^3))	R^2	Maximum Normalized Deviation
1–3 (selected)	0.9223	0.9963	3.52%
1–4	0.8395	0.9918	3.67%
1–5	0.7698	0.9871	5.11%
1–7	0.6565	0.9763	8.27%
1–10	0.5325	0.9589	12.77%

Note: Maximum normalized deviation was calculated as the maximum absolute difference between the simulated response and the fitted regression line, divided by the fitted response span over each concentration interval, and expressed as a percentage. All values were calculated from the COMSOL simulation results at 10 MHz.

4. Discussion

In the present study, a finite element model of an impedimetric biosensor using IDEs for the detection of dengue NS1 antigen was used to investigate the electrical response of the biosensor. The simulation results showed that variations in the electrical properties of the antibody-functionalized biorecognition layer after NS1 binding can lead to measurable changes in the sensor impedance. Furthermore, the electric potential and electric field distributions indicated that the interdigitated electrode geometry has a significant impact on the sensing region. Moreover, the electric field was concentrated around the electrode fingers, especially in the inter-electrode gaps. This field distribution is beneficial for impedimetric sensing, as alterations within the biorecognition layer close to the electrode surface can influence the measured electrical response.

The electrode geometry is an important factor influencing the electrical response of IDE-based impedimetric biosensors. In the present model, the IDE configuration consisted of eight electrode fingers, each 10 μm wide and 100 μm long, with an inter-electrode gap of 10 μm. The simulated electric field distribution showed pronounced field concentrations near the electrode edges and within the inter-electrode gaps, indicating that these regions contribute to the interaction between the electric field and the biorecognition layer. From an electrostatic perspective, reducing the inter-electrode spacing may increase the local electric field strength for a given applied voltage, while changes in electrode width, length, and finger number may influence the effective sensing area, current distribution, and overall impedance. However, these geometrical effects were not independently evaluated in the present study because the electrode dimensions were kept constant throughout the simulations. Therefore, systematic optimization of IDE geometry remains an important direction for future investigation.

For the frequency-dependent analysis, the impedance magnitude was relatively constant at lower and intermediate frequencies, but decreased at higher frequencies. Furthermore, a systematic decrease in the impedance magnitude across the explored frequency range was observed with increasing NS1 concentration. The separation between the impedance curves was maintained at higher frequencies, which supported the choice of 10 MHz for the analysis of the concentration-dependent impedance response. This behavior is a consequence of the frequency-dependent contributions of the dielectric and conductive properties of the sensing interface. The capacitive contribution becomes more significant at higher frequencies, and changes in the effective electrical properties of the biorecognition layer can affect the measured impedance. Under the assumptions of the present model, the results suggest that the operating frequency is one of the key param-

eters to be considered in designing an IDE-based sensing configuration. Although the simulated impedance responses remained distinguishable at 10 MHz, signal stability at the electrode was not explicitly evaluated. The frequency-domain model does not account for time-dependent signal drift, measurement noise, or electrode degradation. Therefore, experimental measurements are required to assess signal stability and repeatability at the selected frequency.

The results showed a nonlinear reduction in the impedance magnitude as the concentration of NS1 increased at 10 MHz. The normalized impedance response increased sharply at low NS1 concentrations and approached saturation at higher concentrations. This trend is consistent with the Langmuir binding model used in the simulation. When the NS1 concentration is low, increasing the concentration causes a relatively large increase in the fraction of occupied antibody binding sites. As the concentration becomes higher, more of the sites are occupied, and the additional increase in surface coverage becomes smaller, resulting in the observed saturation behavior. Hence, the largest relative changes in the simulated impedance response occurred in the low-concentration regime. The simulated decrease in impedance magnitude with increasing NS1 concentration is qualitatively consistent with the experimental findings of Wasik et al., who reported decreasing electrical resistance in an IDE-based NS1 immunosensor [24]. In contrast, Cecchetto et al. and Bachour Junior et al. observed increasing charge-transfer resistance using faradaic electrochemical impedance spectroscopy, highlighting the influence of sensing mechanisms and measurement configurations on the direction of the electrical response [9,25].

The impedance response was normalized and found to have a very good linear relationship with the concentration of NS1 in the range of 1–3 ng/cm^3. Linear regression yielded $R_Z = 0.9223C_{NS1} + 0.3981$, with $R^2 = 0.9963$, corresponding to a simulated sensitivity of 0.9223%/(ng/cm^3). The results suggest a sensor that responds in this low concentration range as a function of concentration. The linear range determined is based on three concentration points and is thus considered a model-derived operating range rather than an experimentally determined analytical range. Further experimental measurements, including additional low-concentration calibration points and replicate measurements, are required to establish the analytical working range and sensitivity of a fabricated sensor.

The simulated concentration range is also relevant when considered alongside previously reported experimental NS1 impedimetric sensors [9,22,23]. However, the results should not be compared directly because the sensing mechanisms, electrode materials, functionalization methods, sample matrices, and response metrics differ among experimental sensors. Cecchetto et al. presented an anti-NS1 label-free gold-electrode impedimetric sensor capable of detecting 3 ng/mL in PBS and 30 ng/mL in serum. Nawaz et al. reported an anti-NS1 screen-printed carbon-electrode immunosensor that achieved a linear range of 1–200 ng/mL and a detection limit of 0.3 ng/mL. Ojha et al. recently reported a Au nanorod–graphitic carbon nitride impedimetric immunosensor that had a linear range of 0.6–216 ng/mL and a detection limit of 0.09 ng/mL in PBS. These experimental studies help to establish the feasibility of NS1 detection using impedance measurements and provide context for the range of concentrations explored in the present computational study. However, the sensitivity obtained in this work should not be interpreted as superior or inferior to that of the experimental devices discussed, due to the significant differences in sensor architecture and measurement techniques.

The present work differs from the experimental optimization of a fabricated immunosensor by focusing on the physics-based investigation of the IDE sensing response. The model provides insights into how NS1-dependent changes in the biorecognition layer modify the electric field distribution and the impedance response over a wide frequency range. This computational analysis can be useful prior to fabrication since parameters such as elec-

trode geometry, excitation frequency, biorecognition-layer properties, and sample-medium properties can be systematically analyzed without the need for repeated fabrication cycles. In particular, the present results suggest that the proposed IDE geometry, combined with high-frequency impedance measurements, warrants further investigation for NS1 sensing.

However, several limitations should be considered when interpreting the results. First, antibody–NS1 binding was modeled using the Langmuir equilibrium model, which assumes homogeneous and independent binding sites. The current model does not represent time-dependent binding kinetics, nonspecific adsorption, or heterogeneous binding that may be observed on real biosensor surfaces. Furthermore, mass-transfer limitations associated with NS1 diffusion toward the sensing surface were not considered, as the binding response was evaluated under an equilibrium assumption. Second, the changes in conductivity and relative permittivity of the biorecognition layer were modeled using effective electrical properties. These properties need to be experimentally characterized, and their quantitative relationship with NS1 surface binding needs to be established. Third, the sample was represented as a homogeneous conductive aqueous solution, while clinical serum or plasma may contain proteins, ions, and other components that may affect the interfacial impedance and lead to nonspecific effects. The influence of fabrication tolerances, electrode surface roughness, temperature changes, noise, and parasitic capacitances was also not taken into account.

Finally, the present study is entirely computational, and the reported impedance response, sensitivity, and linear range represent theoretical predictions rather than experimentally demonstrated analytical performance. Furthermore, analytical performance parameters that depend on experimental measurements and statistical analysis, such as the limit of detection, limit of quantification, selectivity, repeatability, and reproducibility, cannot be determined from the present simulations alone. Experimental fabrication and testing of the proposed IDE sensor are required to verify the predicted impedance trends and sensitivity. Further studies should include the incorporation of experimentally obtained dielectric and conductive properties of the functionalized interface, as well as the investigation of interfering species, evaluation of the sensor in physiologically relevant sample matrices, and comparison of simulated and measured impedance spectra. This validation would help assess the applicability of the model for further optimization of the IDE geometry and operating conditions for dengue NS1 detection.

5. Conclusions

In this study, a finite element model using COMSOL Multiphysics was developed for an impedimetric biosensor for dengue NS1 detection. The model incorporated a Langmuir binding model to describe antibody–NS1 binding and assessed the resulting changes in the electrical response of the sensing interface. Strong electric field localization around the interdigitated electrode fingers and in the inter-electrode gaps was shown by the simulated electric potential and electric field distributions. The frequency-domain analysis showed that the impedance magnitude decreased with increasing frequency and NS1 concentration. The concentration-dependent analysis at 10 MHz showed a nonlinear response that approached saturation at higher NS1 concentrations. A linear fit over three simulated concentration points (1–3 ng/cm^3) yielded a normalized response slope of $0.9223\%/(ng/cm^3)$ ($R^2 = 0.9963$), which should be interpreted as a model-derived estimate rather than an experimentally established sensor sensitivity or linear range. The results demonstrate the potential of computational modeling to characterize the predicted impedance response of an IDE-based biosensor for dengue NS1 detection and guide its future optimization. However, the reported performance is based entirely on numerical simulations and requires experimental validation. Future research will focus on experimental fabrication and validation of

the proposed sensor, characterization of the electrical properties of the biorecognition layer, and testing with physiologically relevant samples to evaluate sensor performance under experimental conditions.

Funding: This research received no external funding.

Institutional Review Board Statement: Not applicable.

Informed Consent Statement: Not applicable.

Data Availability Statement: The data generated and analyzed during the current study are available from the corresponding author upon reasonable request.

Acknowledgments: During the preparation of this manuscript, the author used ChatGPT (GPT-6, OpenAI) for language editing and improvement of the clarity and readability of the manuscript. The author reviewed and edited the output and takes full responsibility for the content of this publication.

Conflicts of Interest: The author declares no conflicts of interest.

Abbreviations

The following abbreviations are used in this manuscript:

DENV	Dengue virus
NS1	Nonstructural protein 1
IDE	Interdigitated electrode
EIS	Electrochemical impedance spectroscopy
FEA	Finite element analysis
PBS	Phosphate-buffered saline
SPR	Surface plasmon resonance

References

1. Hosen, M.E.; Supti, S.J.; Horwood, P.F.; Sarker, S. Adaptive evolution of dengue virus: Interplay between viral genetics and host immunity. *Rev. Med. Virol.* **2026**, *36*, e70082. [CrossRef]
2. Zoladek, J.; Nisole, S. Mosquito-borne flaviviruses and type I interferon: Catch me if you can! *Front Microbiol.* **2023**, *14*, 1257024. [CrossRef]
3. World Health Organization. Dengue. Available online: https://www.who.int/news-room/fact-sheets/detail/dengue-and-severe-dengue (accessed on 1 September 2026).
4. Mohod, S.V.; Supare, S.; Gedam, D.; Agrawal, G.; Solanki, M.V. Temporal trends of dengue among laboratory-referred cases at a tertiary care centre in Vidarbha, Maharashtra: A ten-year retrospective study. *Indian J. Med. Microbiol.* **2026**, *64*, 101264. [CrossRef]
5. Lima, M.R.; Nunes, P.C.G.; Dos Santos, F.B. Serological diagnosis of dengue. In *Dengue Virus: Methods and Protocols*; Humana: New York, NY, USA, 2022; pp. 173–196.
6. Lanciotti, R.S.; Calisher, C.H.; Gubler, D.J.; Chang, G.J.; Vorndam, A.V. Rapid detection and typing of dengue viruses from clinical samples by using reverse transcriptase-polymerase chain reaction. *J. Clin. Microbiol.* **1992**, *30*, 545–551. [CrossRef]
7. Kumarasamy, V.; Chua, S.K.; Hassan, Z.; Wahab, A.H.A.; Mohamad, M.; Chua, K.B. Evaluating the sensitivity of a commercial dengue NS1 antigen-capture ELISA for early diagnosis of acute dengue virus infection. *Singap. Med. J.* **2007**, *48*, 669.
8. Duong, V.; Ly, S.; Try, P.L.; Tuiskunen, A.; Ong, S.; Chroeung, N.; Lundkvist, Å.; Leparc-Goffart, I.; Deubel, V.; Vong, S.; et al. Clinical and virological factors influencing the performance of a NS1 antigen-capture assay and potential use as a marker of dengue disease severity. *PLoS Negl. Trop. Dis.* **2011**, *5*, e1244. [CrossRef]
9. Cecchetto, J.; Carvalho, F.C.; Santos, A.; Fernandes, F.C.; Bueno, P.R. An impedimetric biosensor to test neat serum for dengue diagnosis. *Sens. Actuators B Chem.* **2015**, *213*, 150–154. [CrossRef]
10. Gahlaut, S.K.; Pathak, A.; Gupta, B.D.; Singh, J.P. Portable fiber-optic SPR platform for the detection of NS1-antigen for dengue diagnosis. *Biosens. Bioelectron.* **2022**, *196*, 113720. [CrossRef]
11. Prabowo, M.H.; Chatchen, S.; Rijiravanich, P.; Limkittikul, K.; Surareungchai, W. Dengue NS1 detection in pediatric serum using microfluidic paper-based analytical devices. *Anal. Bioanal. Chem.* **2020**, *412*, 2915–2925. [CrossRef]
12. Purnamasari, A.W.; Alauhdin, M.; Andreani, A.S. A smartphone-assisted paper-based colorimetric biosensor for rapid detection of dengue NS1 antigen. *Diagn. Microbiol. Infect. Dis.* **2026**, *116*, 117558. [CrossRef]

13. Asadi, A.; Ferdosi, F.; Anoosheh, S.; Kaveh, M.; Dadgostar, E.; Ehtiati, S.; Movahedpour, A.; Khanifar, H.; Haghighi, M.M.; Khatami, S.H. Electrochemical biosensors for depression: Diagnosis and therapeutic monitoring. *Clin. Chim. Acta* **2025**, *567*, 120091. [CrossRef]
14. Arishi, W.A.; Eissa, S.; Al-Kattan, K.; Zourob, M. Aptamer-based label-free electrochemical biosensors for the diagnosis of sickle cell anemia. *Biosens. Bioelectron. X* **2023**, *14*, 100389. [CrossRef]
15. da Silva, I.S.; Cardoso, A.R.; Sales, M.G.F. Electrochemical biosensor-based detection assays for early diagnosis of neurodegenerative disorders. In *Smart Diagnostics for Neurodegenerative Disorders: Neuro-Sensors*; Elsevier: Amsterdam, The Netherlands, 2023; pp. 155–177. [CrossRef]
16. Jayanthi, V.S.P.K.S.A.; Das, A.B.; Saxena, U. Recent advances in biosensor development for the detection of cancer biomarkers. *Biosens. Bioelectron.* **2017**, *91*, 15–23. [CrossRef]
17. Wu, C.-C.; Chiang, Y.-H.; Chiang, H.-Y. A Label-Free Electrochemical Impedimetric Immunosensor with Biotinylated-Antibody for SARS-CoV-2 Nucleoprotein Detection in Saliva. *Biosensors* **2022**, *12*, 265. [CrossRef]
18. Ohno, R.; Ohnuki, H.; Wang, H.; Yokoyama, T.; Endo, H.; Tsuya, D.; Izumi, M. Electrochemical impedance spectroscopy biosensor with interdigitated electrode for detection of human immunoglobulin A. *Biosens. Bioelectron.* **2013**, *40*, 422–426. [CrossRef]
19. Zou, Z.; Kai, J.; Rust, M.J.; Han, J.; Ahn, C.H. Functionalized nano interdigitated electrodes arrays on polymer with integrated microfluidics for direct bio-affinity sensing using impedimetric measurement. *Sens. Actuators A Phys.* **2007**, *136*, 518–526. [CrossRef]
20. Ibau, C.; Arshad, M.M.; Gopinath, S.C.; Nuzaihan, M.; Fathil, M.F.M.; Shamsuddin, S.A. Immunosensing prostate-specific antigen: Faradaic vs non-Faradaic electrochemical impedance spectroscopy analysis on interdigitated microelectrode device. *Int. J. Biol. Macromol.* **2020**, *162*, 1924–1936. [CrossRef]
21. Fang, X.; Tan, O.K.; Tse, M.S.; Ooi, E.E. A label-free immunosensor for diagnosis of dengue infection with simple electrical measurements. *Biosens. Bioelectron.* **2010**, *25*, 1137–1142. [CrossRef]
22. Nawaz, M.H.; Hayat, A.; Catanante, G.; Latif, U.; Marty, J.L. Development of a portable and disposable NS1 based electrochemical immunosensor for early diagnosis of dengue virus. *Anal. Chim. Acta* **2018**, *1026*, 1–7. [CrossRef]
23. Ojha, R.P.; Singh, P.; Azad, U.P.; Prakash, R. Impedimetric immunosensor for the NS1 dengue biomarker based on the gold nanorod decorated graphitic carbon nitride modified electrode. *Electrochim. Acta* **2022**, *411*, 140069. [CrossRef]
24. Wasik, D.; Mulchandani, A.; Yates, M.V. Salivary detection of dengue virus NS1 protein with a label-free immunosensor for early dengue diagnosis. *Sensors* **2018**, *18*, 2641. [CrossRef]
25. Bachour Junior, B.; Batistuti, M.R.; Pereira, A.S.; de Sousa Russo, E.M.; Mulato, M. Electrochemical aptasensor for NS1 detection: Towards a fast dengue biosensor. *Talanta* **2021**, *233*, 122527. [CrossRef]
26. Sirivibulkovit, K.; Voelkle, J.; Windisch, D.J.; Muttenthaler, M.; Lieberzeit, P.A.; Saetear, P. Electrochemical Dengue Sensor Based on NS1 Epitope-Imprinted Polymers. *Biosens. Bioelectron.* **2025**, *289*, 117915. [CrossRef]
27. Arena, C.B.; Sano, M.B.; Rossmeisl, J.H., Jr.; Caldwell, J.L.; Garcia, P.A.; Rylander, M.N.; Davalos, R.V. High-frequency irreversible electroporation (H-FIRE) for non-thermal ablation without muscle contraction. *Biomed. Eng. Online* **2011**, *10*, 102. [CrossRef]
28. Hu, D.; Fry, S.R.; Huang, J.X.; Ding, X.; Qiu, L.; Pan, Y.; Chen, Y.; Jin, M.; McElnea, C.; Buechler, J.; et al. Comparison of surface plasmon resonance, resonant waveguide grating biosensing and enzyme linked immunosorbent assay (ELISA) in the evaluation of a dengue virus immunoassay. *Biosensors* **2013**, *3*, 297–311. [CrossRef]
29. Fry, S.R.; Meyer, M.; Semple, M.G.; Simmons, C.P.; Sekaran, S.D.; Huang, J.X.; McElnea, C.; Huang, C.Y.H.; Valks, A.; Young, P.R.; et al. The diagnostic sensitivity of dengue rapid test assays is significantly enhanced by using a combined antigen and antibody testing approach. *PLoS Negl. Trop. Dis.* **2011**, *5*, e1199. [CrossRef]
30. Shriver-Lake, L.C.; Liu, J.L.; Zabetakis, D.; Sugiharto, V.A.; Lee, C.R.; Defang, G.N.; Wu, S.J.L.; Anderson, G.P.; Goldman, E.R. Selection and characterization of anti-dengue NS1 single domain antibodies. *Sci. Rep.* **2018**, *8*, 18086. [CrossRef]
31. Daniels, J.S.; Pourmand, N. Label-free impedance biosensors: Opportunities and challenges. *Electroanalysis* **2007**, *19*, 1239–1257. [CrossRef]
32. Šarolić, A.; Matković, A. Dielectric permittivity measurement using open-ended coaxial probe—Modeling and simulation based on the simple capacitive-load model. *Sensors* **2022**, *22*, 6024. [CrossRef]
33. Farooq, A.; Butt, N.Z.; Hassan, U. Biochip with multi-planar electrodes geometry for differentiation of non-spherical bioparticles in a microchannel. *Sci. Rep.* **2021**, *11*, 11880. [CrossRef]

Disclaimer/Publisher's Note: The statements, opinions and data contained in all publications are solely those of the individual author(s) and contributor(s) and not of MDPI and/or the editor(s). MDPI and/or the editor(s) disclaim responsibility for any injury to people or property resulting from any ideas, methods, instructions or products referred to in the content.